Stringari, C. E.; Harris, D. L.; Power, Hannah E. "A novel machine learning algorithm for tracking remotely sensed waves in the surf zone". Published in Coastal Engineering Vol. 147, Issue May 2019, p. 149-158 (2019).

Available from: http://dx.doi.org/10.1016/j.coastaleng.2019.02.002

A Novel Machine Learning Algorithm for Tracking Remotely Sensed Waves in the Surf Zone

C. E. Stringari[1], D. L. Harris[2], H. E. Power[1]

[1] School of Environmental and Life Sciences, University of Newcastle, Callaghan, NSW, Australia.

[2] School of Earth and Environmental Sciences, University of Queensland, St Lucia, QLD, Australia.

Corresponding author: Caio Stringari (Caio.EadiStringari@uon.edu.au), Hannah Power (hannah.power@newcastle.edu.au)

Keywords: Remote sensing; wave tracking; machine learning; data mining; wave speed; wave celerity

Abstract

This paper describes a novel image processing technique that detects wave breaking and tracks waves in the surf zone using machine learning procedures. Using time-space images (timestacks), the algorithm detects white pixel intensity peaks generated by breaking waves, confirms these peaks as true wave breaking events by learning from the data's true colour representation, clusters individual waves, and obtains optimal wave paths. The method was developed and tested using data from four sandy Australian beaches under different incident wave and light conditions. Results are a representation of the position of the wave front front through time, i.e., space-time data, which when shown overlaid on the original timestack shows the high degree of accuracy of the method developed here. The utility of the method is demonstrated in two ways: 1) through a comparison between the instantaneous wave speed calculated from the wave paths with the theoretical shallow water wave speed, and 2) by obtaining optical intensities that could be translated into wave roller lengths. The algorithm developed here has the potential to improve understanding numerous nearshore process such as bore propagation and capture in the surf zone,

surf zone energy dissipation, surf beat and infragravity waves, and as a direct speed input for depth inversion methods.

1 Introduction

Wind-generated gravity waves are the main driver for nearshore dynamics (Komar, 1998; Battjes, 1998). In particular, surf and swash zone processes have a significant impact on the subaqueous-subaerial nearshore boundary, and are the primary driver of sediment exchange in this region (Masselink and Puleo 2006). Several recent studies have focused on wave-by-wave (Power et al., 2010; Postacchini and Brocchini, 2014; Martins et. al, 2017b) or swash-by-swash (Power et al., 2011; Padilla and Alsina, 2017; Martins et al., 2017a) approaches to investigate nearshore phenomena, but have found high variability for nearly all processes investigated (e.g., Power et al., 2010; Power et al., 2011; and Martins et al., 2017a). Such results suggest that, even under laboratory conditions, the full the evolution of shallow water waves on a wave-by-wave scale must be considered in order to understand the full wave transformation in the nearshore.

Very few studies have tracked the evolution of individual waves across the surf zone of natural beaches. To the authors’ knowledge, only Suhayda and Pettigrew (1977), Yoo et al. (2011), and Power et al. (2015) have made attempts. Suhayda and Pettigrew (1977) used a method in which individual waves were videoed and visually compared to wave poles in the surf zone. Such a method has the disadvantage of being extremely labour intensive and is thus only suitable for tracking a few waves. Yoo et al. (2011) used the Radon transform to track individual waves on timestack images (see Aagaard and Holm, 1989), but only presented results for averaged wave conditions which may not account for the full variability of wave heights and speeds seen in the surf zone. More recently, Power et al. (2015) tracked waves using closely spaced arrays of pressure transducers (PTs) deployed in the surf zone. This method has the advantage of tracking parameters such as the wave height (H) and the local water depth (h) but was sensitive to the definition of the temporal searching window which could lead to a different number of waves being tracked.

To address the difficulties in tracking individual waves, and thus to further understanding of the variability observed in surf and swash zone processes, this paper describes a novel algorithm for tracking waves in the surf zone that uses computer vision, peak detection, and machine learning techniques. The method is similar in concept to the method of Power et al. (2015) in that it tracks peaks in timeseries in a cross-shore orientation, however, the method presented here uses data derived from coastal video imagery instead of PT measurements. The algorithm exploits the fact that colour signature of breaking waves is significantly different to the colour signature of calm water, unbroken waves, or sand. This colour signature of breaking waves is seen as white pixel peaks in timeseries extracted from timestacks. When these peaks are clustered and tracked using machine learning methods, it is possible to fully track the paths of breaking waves in the surf zone. The method derived here gives similar results to the Radon transform method of Yoo et al. (2011) and Almar et al. (2014) but can be directly applied to any timestack image without the need of complex transforms (e.g., Radon or Hough transforms), thus greatly reducing computation costs and analysis complexity. More importantly, the method described here is, to the authors' knowledge, the only method capable of automatically tracking the occurrence of wave overrunning (bore merging) in the nearshore.

This paper is organized as follows: Section 2.1 describes the study sites, data collection methods and datasets to be investigated, and Sections 2.2 and 2.3 describe how wave breaking events are detected, confirmed, and tracked. Section 3.1 presents the results in the forms of the obtained wave paths overlayed on to the original timestacks, and a comparison to the Yoo et al.'s (2011) method. Sections 3.2 and 3.3 present brief examples of applications of the method: in

Section 3.2, the instantaneous wave speed is directly obtained from the wave paths, and in Section 3.3, phase-averaged optical intensities are obtained and compared to Haller and Catálan's (2009) results. Section 4 discusses of the results presented in Section 3, and conclusions are given in Section 5.

2 Methods

2.1 Field data

Video imagery of the nearshore was collected at four different News South Wales (NSW) beaches covering different wave breaking, light, and grazing angle conditions (Figure 1 and Table 1). For each experiment, a consumer-grade high-resolution video camera (Sony HDR-CX240) recorded the surf and swash zones at 25 frames per second from an elevated location (headland or a house balcony) for several hours. All study sites were surveyed at low tide using a total station to obtain a beach profile and at least four ground control points (GCPs) per site. The coordinate system for all data was such that the PT line is cross-shore oriented (positive seaward); the video and survey data were adjusted accordingly. Beach profiles were surveyed from the location of the first foredune to the maximum depth possible, limited by wave breaking conditions. The beach slope ($tan\beta$) was calculated across the surf and swash zones from the beach berm to the end of the profile. Transformed spectral offshore wave parameters (significant wave high, peak period and mean wave direction) were obtained from the NSW Nearshore Wave Forecast toolbox (NSW-OEH, 2017) at the nearest 10m isobath. The surf zone spectral wave height (H_{m0}) and period (T_{m01}) were calculated from data measured by a PT deployed in the mid to outer surf zone using the methods of Holthuijsen (2007). Additionally, a cross-shore array of evenly spaced PTs was deployed in the surf and swash zones along the timestack transect (Figure 1 and Table 1).

Three of the four study sites are classed as intermediate beach states in the Australian morphodynamic beach model (Wright and Short, 1984), which is the most frequently occurring beach state for microtidal, swell-dominated Australian beaches. During the data collection period, One Mile Beach (OMB, Figure 1-a) had a low tide terrace morphology with rhythmic beach cusps, and plunging breakers. Werri Beach (WB, Figure 1-b) had a steep beach profile, especially the beach face, low tide terrace morphology (without apparent rhythmic beach cusps), and plunging breakers. Birubi Beach (BB, Figure 1-d) had a very gently sloping profile, one longshore bar, and spilling breakers. Seven Mile Beach, Gerroa, (SMB, Figure 1-c), was the only dissipative study site, and had a gently sloping profile, no apparent longshore bars or troughs, and spilling breakers. Reflective beaches were not considered because of the absence of wave breaking before the outer limit of the swash zone, which precludes them from any significant surf zone data collection.

The light conditions and camera grazing angles varied between the experiments. OMB and WB were imaged from elevated headlands with clear sky conditions. SMB was imaged from a house balcony located on the elevated peninsula to the north of the beach with a shallow grazing angle and had moderately overcast conditions, which resulted in low-contrast images. BB was recorded from a non-ideal grazing angle (very shallow) with clear skies, which resulted in a large amount of specular reflection, particularly in the swash zone. The BB experiment also had strong winds throughout the duration of the experiment, which resulted in large amounts of foam in the surf zone, making wave paths less defined.

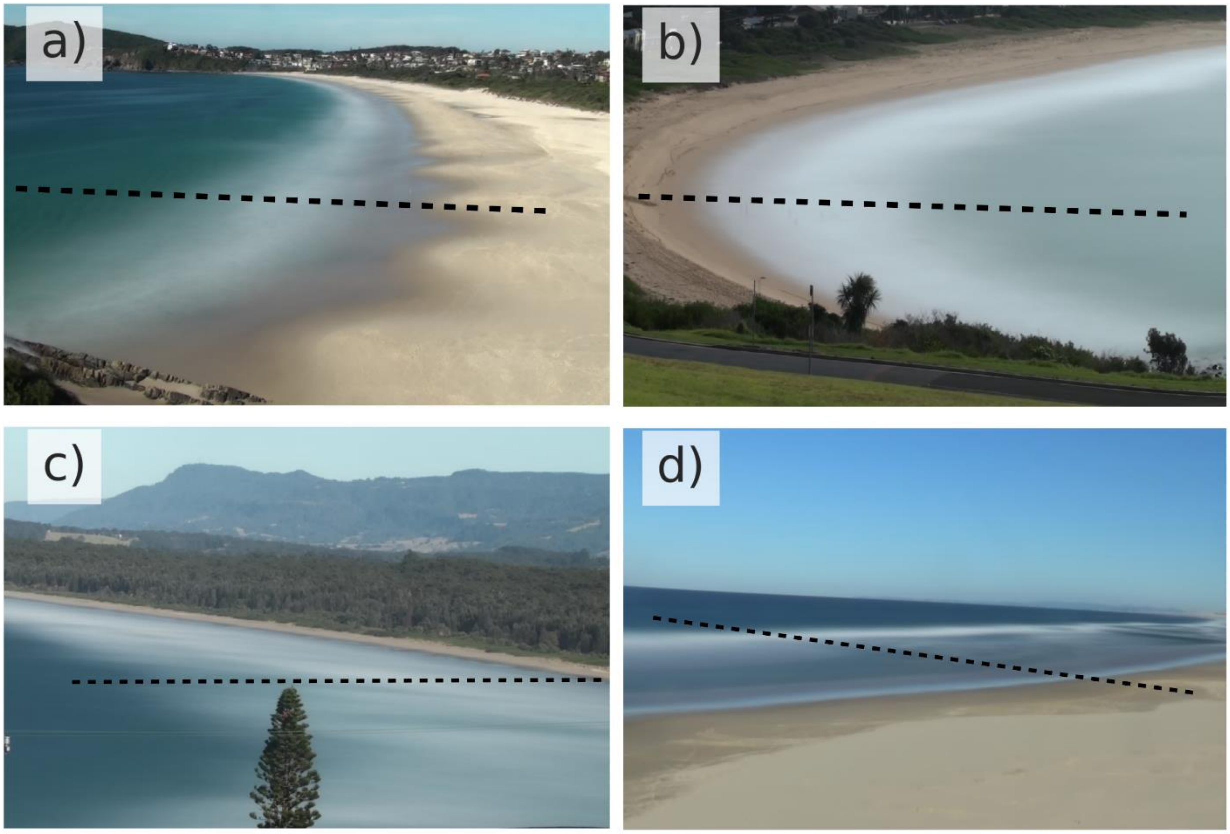

Figure 1. *Time averaged (Timex) images for the four data collection sites: a) One Mile Beach (OMB), b) Werri Beach (WB), c) Seven Mile Beach (SMB), and d) Birubi Beach (BB). All Timex images were calculated from 10 minutes of video data resampled at 2Hz following Holland et al. (1997). The black dashed lines indicate the timestack and PT transect locations.*

Table 1. *Data for each beach: location, date of the experiment, total number of PTs (nPT) deployed, PT array cross-shore spacing (dx), beach slope (tanβ) from the berm to the end of the profile, offshore significant wave height (H_{m0_∞}), offshore peak period (T_p, offshore mean wave direction (D_m), Offshore Iribarren number ($\xi_o = tan\beta / \sqrt{H_{m0_\infty} / \left[(g/2\pi) * T_p^2\right]}$), spectral*

significant wave height in the surf zone (H_{m0}), spectral significant wave period in the surf zone (T_{m01}), and observed breaker type.

Location	**Date**	**nPT**	**dx (m)**	**tanβ (-)**	H_{m0_∞} **(m)**	T_p **(s)**	**D_m (°)**	**ξ_o (-)**	**H_{m0} (m)**	**T_{m01} (s)**	**Breaker (observed)**
One Mile Beach	07/08/14	12	3	0.076	0.98	13.8	E	1.32	0.81	9.37	plunging
Seven Mile Beach	13/08/14	12	10	0.03	1.18	12.7	SE	0.44	0.57	7.98	spilling
Werri Beach	16/08/14	13	3	0.355	0.96	7.8	SE	3.53	0.92	8.26	Heavy plunging
Birubi Beach	06/07/17	9	6	0.02	0.78	8.4	S	0.12	0.43	10.24	Spilling/weak plunging

2.2 Wave breaking detection

All video imagery was pre-processed following Holland et al. (1997) using the algorithm of Hoonhotut et al. (2015). To ensure a high temporal resolution for wave tracking, the camera data were downsampled to 10Hz instead of the usual rate of 2Hz that is most frequently used in the literature. Each frame was projected into metric coordinates and frames were grouped into five minutes batches, the optimal duration for this analysis. From these frame batches, a cross-shore array of pixels was extracted and stacked in time (dashed black lines in Figure 1 and Figure 2-b), resulting in an image known as timestack (Aagaard and Holm, 1989) (Figure 2-a). Using these timestack images, two methods were developed to identify wave breaking depending on the breaker type. Firstly, for spilling and plunging breakers, pixel intensity timeseries were extracted every 10cm in the cross-shore direction (with sub-pixel accuracy) and pixel peaks were identified using a peak detection algorithm that iteratively searches for local extrema in the timeseries. Pixel intensity local maxima were found to closely correspond to white pixels generated by foam corresponding to the crests of breaking waves (Figure 2-c). Secondly, for strongly plunging breakers, wave breaking was detected as sharp pixel intensity transitions in the timestack by applying the horizontal Sobel operator (Sobel, 1968) and tracking the location of the resulting edges in the cross-shore orientation by obtaining the argument of the maxima of the detected edges at every timestamp. The second method was developed in order to track the exact front edge of the wave in cases where the original local maxima method showed high sensitivity to the white signatures of residual foam in the surf zone, which was more problematic in the detection of heavy plunging breakers.

In most cases, the identified pixel peaks directly corresponded to white foam associated with breaking wave crests; however, there were several instances where specular light reflection both offshore and in the swash zone was incorrectly identified as wave breaking (Figure 3-a). To avoid such misclassifications, all identified peaks were confirmed as true breaking waves (i.e., white foam) by a machine learning algorithm that obtained information from the timestack's true colour representation (i.e., from the raw RGB values). The training dataset for this algorithm was created by manually defining regions in the timestack that corresponded to breaking waves, sand, and undisturbed water (i.e., unbroken waves). Each training region was defined once for each location from the first five minute data batch using a Graphic User Interface (GUI) built in the tracking algorithm and was re-used for all subsequent data batches. For each of these regions, a dominant colour was obtained using a colour quantisation procedure (Celebi, 2011), and the previously identified pixel peaks were tested against these colours (Figure 4-d). For an identified pixel peak to be confirmed as a true wave breaking event, its true colour needed to be more than 50% similar to the dominant colour of the wave breaking region defined in the training dataset.

The metric used for the comparison was the colour similarity (ΔE^*) calculated using the CIE (International Commission on Illumination) standard computed in the CIECAM02 (CIE Color Appearance Modelling for Color Management Systems) colour space (CIE, 2017). The metric ΔE^* is a direct measurement of how different (or similar) two colours are, and it is calculated as the Euclidian distance between these two colours in an appropriated colour space. In the simplest case, the RGB (Red, Green and Blue) colour space, it is written as:

$$\Delta E^* = \sqrt{(R_1 - R_2)^2 + (G_1 - G_2)^2 + (B_1 - B_2)^2} \quad (1)$$

in which the subscripts 1 and 2 represent two different colours. Simpler, non-perceptual, colour spaces (e.g., RGB and XY; Smith and Guild, 1931) do not correspond directly to the way humans perceive colour because the human eye has a lower tolerance to some colours (particularly blue shades) causing the Euclidian distance to not to be perceived uniformly across the colour space (Lou et al., 2006, CIE2007). To avoid this issue, the more sophisticated CIECAM02 colour space, which is perceptually uniform and should thus closely correspond to the human colour perception (Lou et al., 2006), was used instead. Therefore, the algorithm described here mimics the human perception of breaking wave crests as seen in the timestack images.

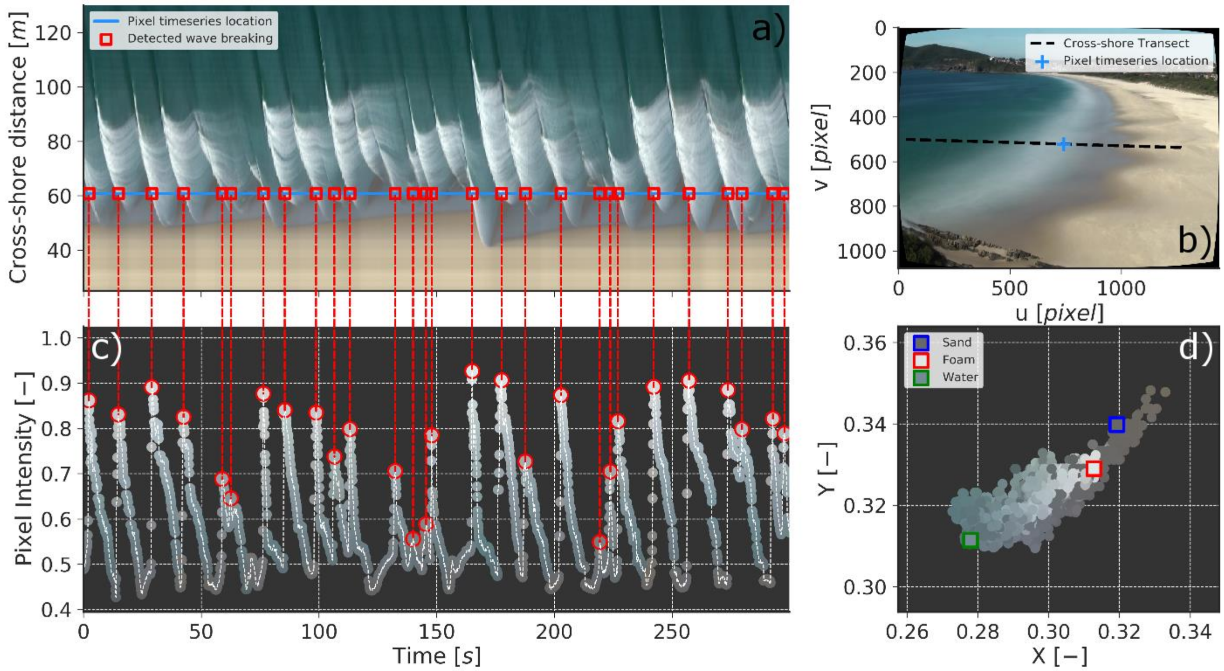

Figure 2. *Example of the wave breaking detection process. a) Subset (300s) of a timestack generated from data collected at One Mile Beach. The continuous blue line indicates the cross-shore location where the timeseries shown in c) was extracted for the pixel peak detection and colour classification. The red squares show the space-time occurrence of the wave breaking events as identified by the machine learning procedure. b) Timex image calculated for the same time period shown in a). The black dashed line indicates the cross-shore transect along which the timestack shown in a) was extracted, and the blue cross indicates the location where the timeseries shown in c) was extracted. c) Pixel intensity timeseries coloured using the corresponding true colour values. The red markers indicate the pixel peaks that correspond to broken waves as identified by the machine learning procedure. d) Pixel data from c) represented in the XY (Smith and Guild, 1931) colour space (for illustration purposes only) showing the corresponding*

dominant colours for each region (sand, foam, and undisturbed water) which were used to assess the pixel peaks identified breaking waves.

2.3 Wave tracking

The peak detection and classification step described above produces a point-cloud-like representation of wave breaking events in the space-time domain (red circles in Figure 3-a), i.e., it does not allocate pixel peaks to a particular wave. To group pixel peaks that correspond to a single wave and to effectively track that wave, the DBSCAN clustering method (Esther et al, 1996) was used (Figure 3-b). This unsupervised classification method clusters data based on two criteria: 1) the distance between each data point (eps), and 2) the minimum number of points required to form a cluster (n_{min}). Before applying the algorithm, the data were transformed to scaled coordinates by dividing the time (space) occurrence of each breaking event by the total length along the time (space) axis. This was done as a requirement for using the distance metrics implemented in the DBSCAN algorithm. As the algorithm is not optimized to work with wave data, it occasionally grouped two different waves into one cluster if the distance criterion was met. Another issue with the DBSCAN algorithm was that instances of bore merging/captures were always grouped as one cluster. For cases where two waves merged with a clear separation between the two wave paths, (e.g., wave 6 in Figure 3-b), it was possible to split the wave paths using the Random Sample Consensus (RANSAC) estimator (Fischler and Bolles, 1981). In this technique, the points forming one wave path were identified as being inliers whereas the points of the secondary wave were identified as outliers, enabling the cluster to be split into two separate clusters. Other clustering errors (e.g., waves 5 and 27 in Figure 2-b) were manually fixed in QGIS using data exported from the wave paths into an appropriate file format (ESRI® shapefiles). The procedures described in Sections 2.2 and 2.3, as a well the functionality to export and import data into QGIS, were coded in Python and rely heavily on the Scikit-Learn (Pedregosa et al, 2011) and Open-CV (ITSEEZ, 2014) packages for machine learning and computer vision, respectively. The code and a sample dataset (OMB) are available at https://github.com/caiostringari/pywavelearn[1].

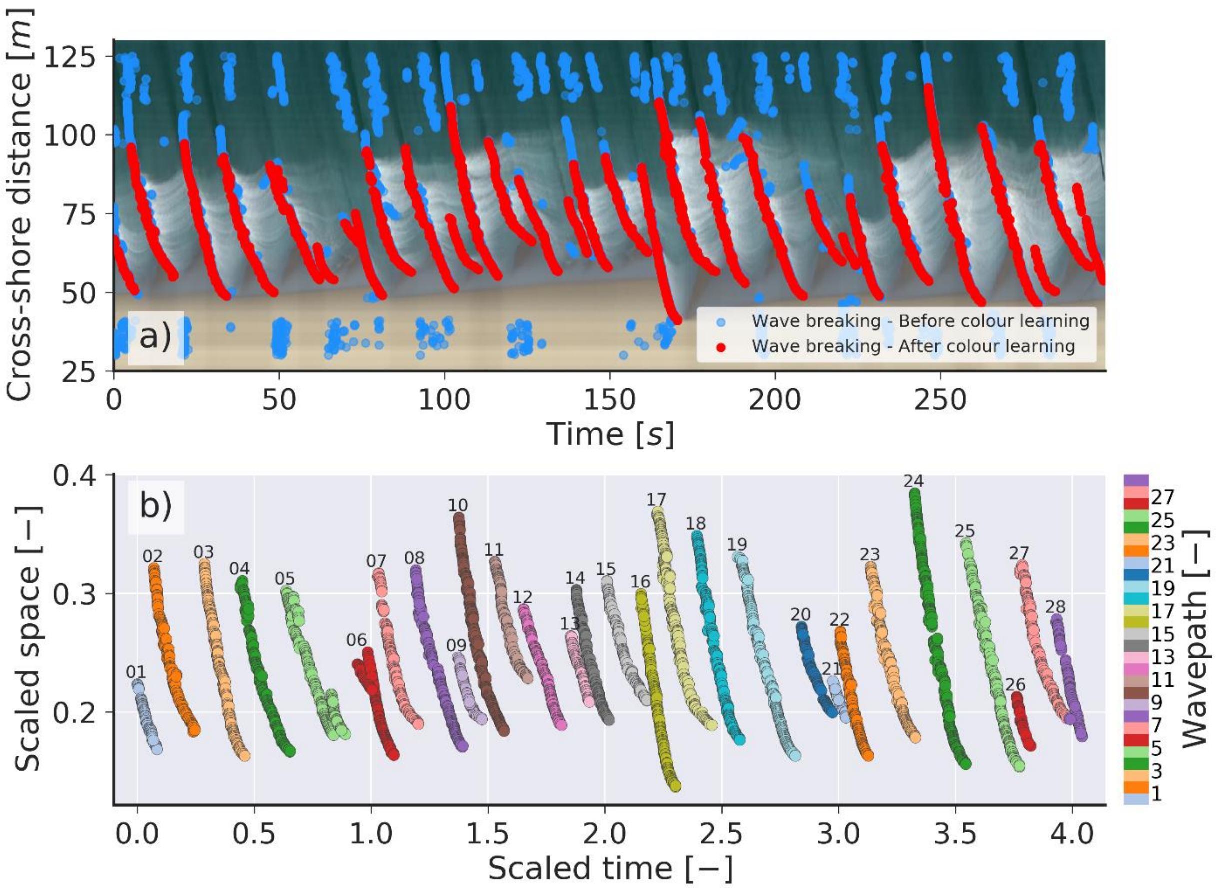

Figure 3. *Conversion of point could data to grouped waves. a) Wave breaking events in the time-space domain before (blue and red markers) and after (red markers) the machine learning procedure. These data are initially not assigned to any wave. b) Points clustered into discrete wave events whereby the clustering is done based on the squared Euclidian distance between each point*

[1] The repository is currently in private mode. It will be made public available once the paper is accepted for publication. Before publication, access can be granted upon contacting the first author with an email informing a valid GitHub account, or contacting the first author directly via GitHub at https://github.com/caiostringari.

and the minimum number of members in a cluster (eps=0.005 and $n_{min=}$*15, in this example). Each cluster represents a unique wave traveling shoreward (excluding bore-merging events).*

For further analyses, it was useful to obtain a continuous representation of each wave path. This was done by interpolating the detected breaking events in each cluster to a target frequency (2Hz) using a quadratic spline interpolator, and fitting a (minimum) second-order ordinary least-squares (OLS) model. A confidence interval (CI) for each wave path was also defined to account for the uncertainties from both the wave breaking detection and interpolation steps. Two criteria were used to define these confidence intervals. The first criterion considered the curve defined by the OLS model ± one quarter of the standard deviation in both time and space. The second criterion, which was only used in the cases where the standard deviation in time was less than one second, added a buffer of 0.5s to each side of the curve defined by the OLS model. The definition of second method was necessary in order to create a CI for very short-period waves that had no significant standard deviations in either time or space, and to keep the method's consistency. Examples of the continuous wave paths defined by the OLS model (coloured lines) and the confidence intervals (solid lines) are shown in Figure 4.

3 Results

3.1. Wave tracking

Figure 4 shows examples of the results produced by the tracking algorithm applied to the datasets shown in Figure 1. The algorithm tracked individual waves in the surf and swash zones efficiently and accurately in all four cases. For OMB, SMB, and BB datasets, the algorithm was set to track local maxima in the cross-shore pixel intensity timeseries, whereas for WB, the Sobel version was used due to the strong plunging characteristics of the breakers during the experiment.

Varying the peak detection algorithm (local maxima or Sobel edge detection) resulted either in similar results (e.g., OMB dataset), or completely wrong results (See Section 4). The method performed well even under low-contrast (SMB) and non-optimal grazing angles (SMB and BB), and the machine learning step of the algorithm could correct falsely identified intensity peaks in the majority (>90%) of the cases (e.g., Figure 3-a).

A comparison between the number of waves in the surface elevation record (see Figure 5b) and the number of waves tracked from the video imagery during a one hour interval at all locations was also carried-out. Considering all waves (broken and unbroken) in the PT records, the algorithm tracked, in average, 75% of the waves. When the one third highest waves are considered (i.e., waves which $H \geq H_{m0}$), the algorithm tracked the vast majority of the waves (average of 97.25%), and when the 10% highest waves are considered ($H_{1/10}$), the algorithm tracked all waves. Table 2 shows the results of this analysis sorted by location. However, it should be noted that this comparison is not expected to produce directly comparable results because it compares two different types of waves: tracked waves (i.e., broken waves) and all waves (i.e., broken and unbroken waves).

In comparison to the method of Yoo et al. (2011), the method developed here tracks 30% more waves, and represents a significant improvement in the number of breaking points detected. In fact, from visual inspection, the vast majority (>95%) of the breaking points were detected due to the algorithm's capability to learn colour transitions (blue to white). In comparison, Yoo et al's., (2011) method only detected 42% of the breaking points.

Table 2. *Comparison between the number of waves in the PT record and the number of waves tracked by the algorithm in each location during a one hour interval.*

Location	Birubi Beach	One Mile Beach	Seven Mile Beach	Werri Beach
N. PTs in the surf zone	7	4	4	3
N. of waves (all PTs)	1970	1495	1309	1236
% Tracked Waves	72%	79%	76%	75%
% Trac. W. $H \geq H_{m0}$	98%	97%	96%	98%
% Trac. W. $H \geq H_{1/10}$	100%	100%	100%	100%

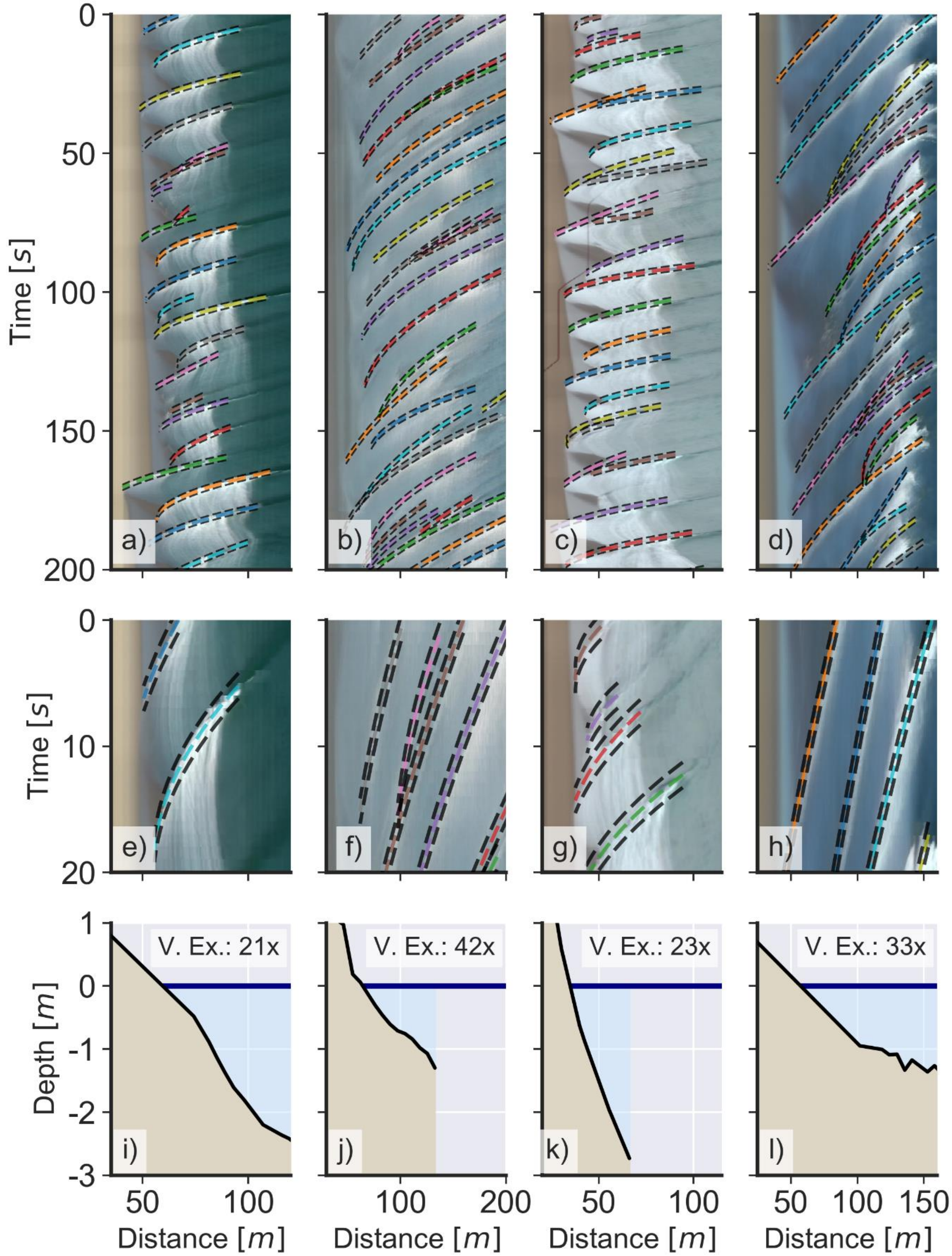
Time [s]
0
50
100
150
200
a)
b)
c)
d)
0
10
20
e)
f)
g)
h)
Depth [m]
1
0
-1
-2
-3
V. Ex.: 21x
V. Ex.: 42x
V. Ex.: 23x
V. Ex.: 33x
i)
j)
k)
l)
50 100
100 200
50 100
50 100 150
Distance [m]

262

Figure 4. *Results of the wave tracking algorithm for: a) One Mile Beach. b) Seven Mile Beach. c) Werri Beach. d) Birubi Beach. Panels from e) to h) show a subset of 20 seconds for the same locations as in a) to d). The dashed coloured lines show the unique wave paths defined by the OLS model after corrections using the RANSAC estimator and minimal manual fixes. The black dashed lines show the confidence intervals for each wave. Panels i) to l) show the beach profile and the mean water level during the experiment (thick blue line). Note that the vertical exaggeration (V. Ex.) varies between panels.*

3.2 Instantaneous surf zone wave speed

To illustrate of the potential of the method developed here, results for the observed instantaneous surf zone wave speed are presented for a one hour subset of collocated PT and video imagery from the OMB dataset. This dataset was chosen because it had a high grazing angle, clear skies, and, more importantly, because it had the lowest rectification errors (average of 0.11m calculated based on back-projection of GCPs). Using the wave paths defined by the OLS model, the instantaneous wave phase speed (c_{wp}) can be calculated as

$$c_{wp} = \lim_{\Delta t \to 0} \left(\frac{\Delta x}{\Delta t}\right) = \frac{dx}{dt} \quad (2)$$

where Δt is the time interval between two measurements and Δx is spatial displacement of the wave front. Figure 5-a shows the results of Equation 2 applied to the OMB data subset (see Table 1 and Figure 4-a).

As the video timestacks were collocated with the PTs deployed in the surf zone, it was possible to identify both the velocity calculated from the remotely sensed wave paths and the water depths recorded in situ by the PTs. For each five-minute batch of data, the wave paths were linked to the matching individual waves in the pressure transducer record that were obtained using a local extrema analysis following Power et al. (2010) (Figure 5-a and b, red markers and dashed connection lines). Although the camera and the PTs clocks were synchronized before the deployment, a residual delay between the two datasets (usually between 1 and 10 seconds) was observed in all datasets. This time difference was primarily due to small differences between the camera clock and the PT clocks introduced in the programing stage which unfortunately were not fully accounted for in the synchronization step. To optimize the alignment between the peaks in the pressure record and the wave paths, an averaged optimal time delay for each data run was obtained using a cross-spectral analysis and then the PT timeseries was shifted to align with the timestack.

The wave speed calculated from Eq. 2 was then compared to the wave crest (h_{cr}) and trough depths (h_{tr}) (Figure 5-c and d). The results showed that the crest depth accounted for more variability (relatively, 55% more) than the trough depth. In addition, a comparison between the calculated wave speed and the theoretical shallow water wave speed ($c_{th} = \sqrt{g(h+\eta)} = \sqrt{gh_{cr}}$ where h is the mean water depth, and η is the instantaneous water surface elevation) was carried out. Only data seaward of the surf-swash boundary were considered in this analysis (see Figure 5-a). The surf-swash boundary was obtained directly from the timestack as the lowest observed rundown in each 5min data batch. Figure 5-e showed that the theoretical wave speed was only partially correlated (68%) to the optically derived wave speeds. The correlation coefficients were calculated on unbinned data using the Pearson product-moment correlation coefficient (r_{xy}) and a two-tailed normal distribution for p values. The observed root mean square error (RMSE) was of 0.69 m.s^{-1}, the mean absolute error was 0.55 m.s^{-1}, and there was virtually no bias (-0.002 m.s^{-1}).

To validate the results shown in Figure 5-e, the difference between the time of travel of individual waves in the PT record and in the wave paths was calculated for two adjacent PTs (at x=84m and x=81m) was calculated (Figure 6-a). The mean absolute error for this analysis was 0.25s, which is six times smaller than the threshold used by Power et al. (2015) to distinguish between individual waves in the surf zone using PT data only, and falls within the confidence intervals for the wave paths shown in Figure 4-a. In addition, the mean time of travel was 0.63s for both PT and wave path, thus resulting in the same averaged wave speed for both datasets (4.74 $m.s^{-1}$). No significant trends or biases were observed when this analysis was performed (see Figure 6-b).

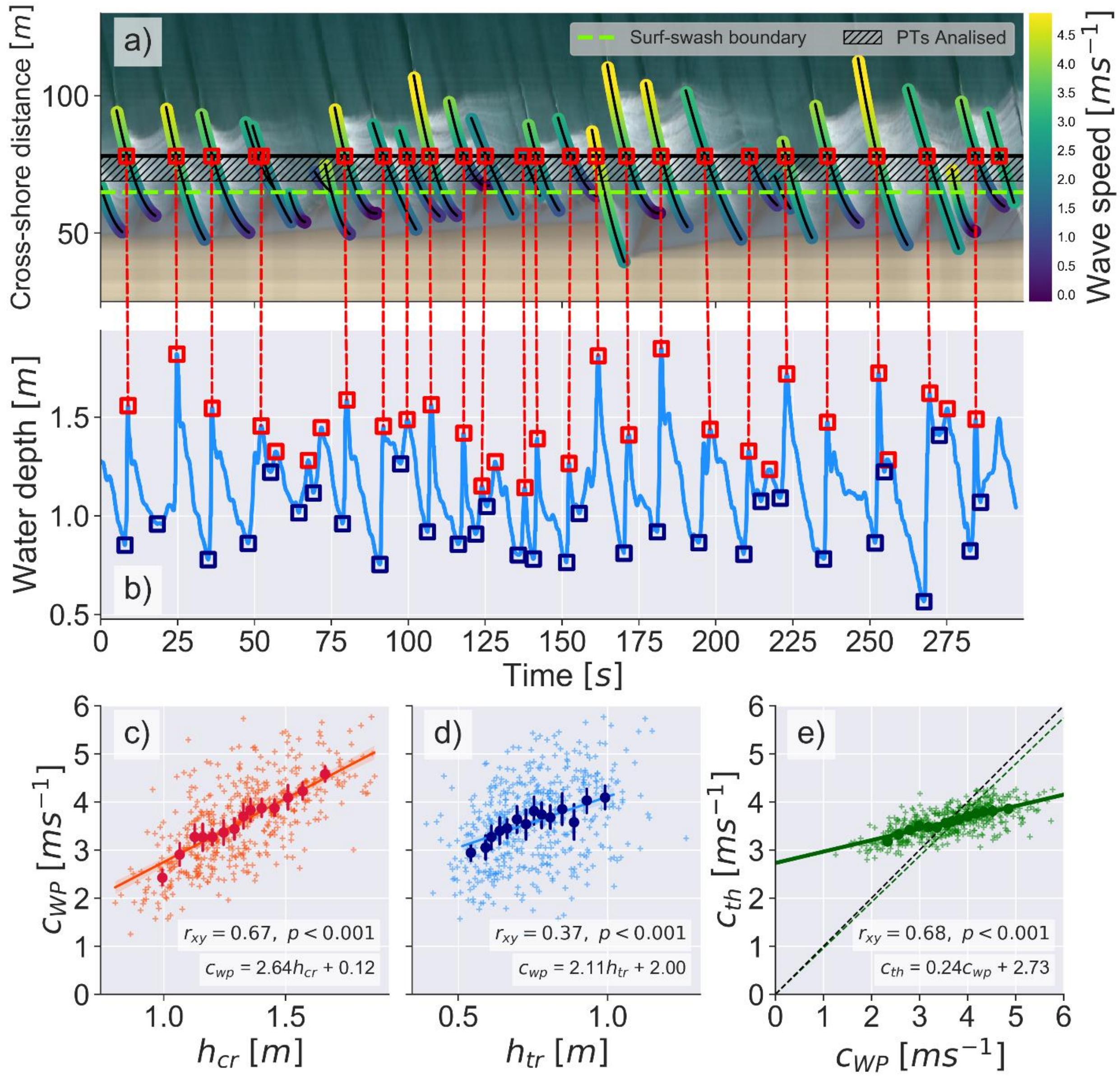

Figure 5. *a) Example of the instantaneous wave speeds calculated using Equation 2 for five minutes of data collected at OMB. The black line represents the location of the PT used in b), the hatched area represents the region from where PT data were obtained for the analyses in c), d) and e), and the dashed green line shows the surf-swash boundary. b) Pressure transducer timeseries data collected at OMB for the same time interval. The blue squares represent the local minima, and the red squares the local maxima obtained from a wave-by-wave analysis following*

Power et al. (2010). The dashed red lines indicate the optimal alignment between the timestack tracked wave crests and the wave crests from the wave-by-wave analysis. c) Comparison between the wave speed (c_{wp}) and the crest depth (h_{cr}) obtained from the PT deployed at x=78m. d) Comparison between the wave speed (c_{wp}) and the trough depth (h_{tr}). e) Comparison between the measured instantaneous wave speed (c_{wp}) and the theoretical shallow water wave speed ($c_{th} = \sqrt{g(h+\eta)}$) for one hour of data for four PTs spaced 3 meters apart starting at the PT at x=84m in the shoreward direction. Data are binned to aid visualisation and the number of bins was calculated following the Freedman-Diaconis rule (Freedman and Diaconis, 1981). The dashed black line in e) shows the one-to-one correspondence, and the dashed green line shows a linear regression to the data without consideration of an intercept term. In c) d), and e), r_{xy} is the Pearson product-moment correlation coefficient and p was calculated using a two-tailed normal distribution. All regressions shown in Figure 5 used unbinned data.

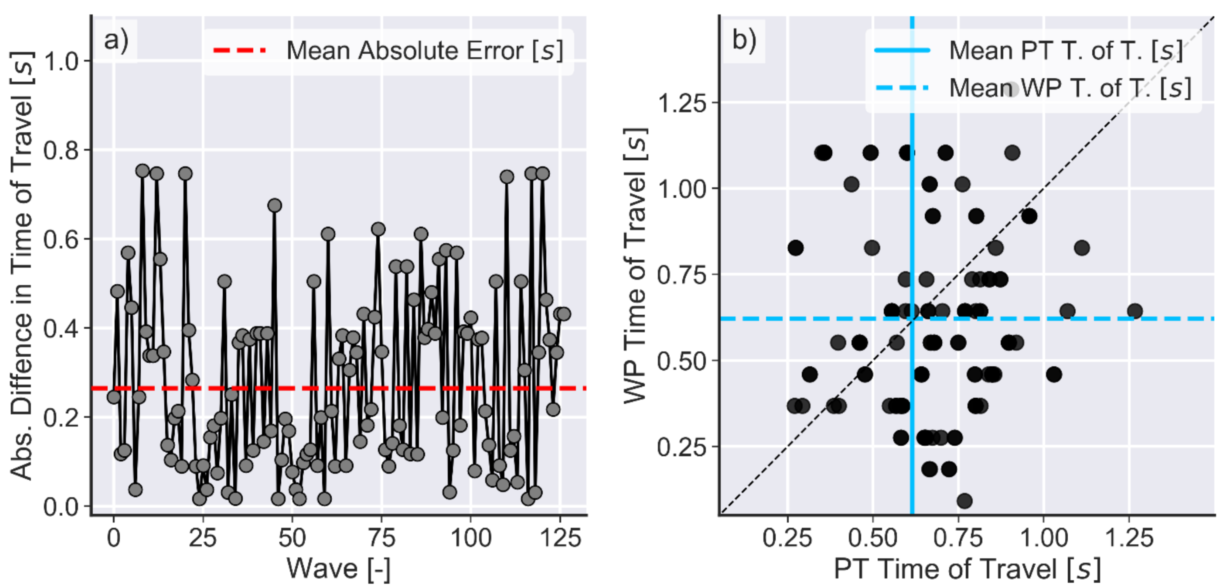

***Figure 6**. a) Absolute difference in time of travel between individual waves in the based on two adjacent PTs (x=84m and x=81m) and based on the wave paths at the same location. b)*

Comparison between the times of travel calculated based on the PT and on the WP data (black markers). The dashed black line in b) shows the bisector.

3.3. Optical intensities of breaking waves

Another application of the algorithm developed here is to obtain the optical intensities of the breaking waves which can be translated into wave roller lengths, as per the method of Haller and Catálan (2009). This method relies on phase-averaging pixel intensity timeseries in both time and space and projecting these intensities into the timestack domain in order to obtain wave roller lengths. Under laboratory conditions, and for a narrow bandwidth wave spectrum, the optical intensities correlate very well with surface elevation data (η) thus justifying the application of the method (Haller and Catálan, 2009; their Figures 4 and 5). However, the same authors suggested that for natural surf zones, where the wave spectrum bandwidth is typically broader than in a laboratory context, a more sophisticated means of wave tracking would be needed to perform a similar analysis. The method developed here has the required characteristics to enable a similar analysis to be carried out on natural surf zone data.

Using the data described in Section 3.2, optical intensities were initially extracted at three cross-shore locations (Figure 7a - 78m, 81m and 84m). At each location, a buffer of 2.5 meters in the cross-shore orientation was used to extract and average optical intensity timeseries in order to remove short-period period oscillations (similar to the method of Haller and Catálan, 2009; their Figure 2). These cross-shore locations coincided with the locations of three PTs from which individual wave pressure time series were extracted following the method of Power et al. (2010) (See Figure 5-a). Each individual wave was then interpolated to a regular grid, normalized by its period (T), shifted so that all crests are aligned, and the median wave profile was obtained for each PT (Figure 7-b, c, and d). For each individual wave in the PT data, an analogue timeseries was extracted from the optical intensity data. In order to ensure that the surface elevation and pixel intensity timeseries were aligned as best as possible (i.e., so that the time delays seen in Figure 6-b are minimised), a wave-by-wave optimal time delay was obtained via cross-correlation analysis and, if needed, the pixel intensity timeseries was shifted in order to match the PT data. From these individual optical timeseries, a median intensity profile was calculated (Figure 7-e, f, and, g). In contrast with Haller and Catálan (2009), the field data shown here did not show a strong match between the optical intensities and the median water surface profile. This occurs because in natural surf zones, with a random wave field, each individual wave is at a different stage of evolution at any given cross-shore location (e.g., the waves between 50s and 100s in Figure 7-a).

To minimize the variability seen in the optical intensities at fixed cross-shore locations (i.e., Figure 7-b), the same analysis was repeated at equivalent locations along the individual wave propagation pathways across the surf zone. This was done by obtaining the length of the wave propagation path from the break point to the bore collapse for each individual wave and using this to define comparable hydrokinematic locations for each individual wave (Svendsen et al., 1976). Three locations were investigated: 1) the breakpoint (defined as 5% of the wave path length after the break point location; Figure 7-a, orange markers), 2) the mid-point of wave transformation across the surf zone (50% of the wave path length after the breakpoint location; Figure 7-a, blue markers), and 3) the point immediately prior to bore collapse (95% of the wave path length after the break point location or 5% of the wave path length before the point of bore collapse (Figure 7-a, green markers). The points of bore collapse were manually defined using the QGIS data exchange interface described in Section 2.3. At each of these locations, and for each wave, 15s optical intensity timeseries with the centre of wave path at one-third of the wave duration were extracted and then phase-averaged to obtain a median optical intensity (Figure 7-h, i, and j). This time interval was chosen to cover the temporal evolution at a given hydrokinematic location but does not necessarily represent the period of individual waves due to the random characteristic of the wave field. It was used instead of the normalised wave period also because there was no clear way to define wave periods based only on the pixel record since the local minima in the pixel record does not necessary correspond to wave troughs.

In comparison to Haller and Catálan’s (2009) method (which relies on a regular wave field and thus a given distance consistently represents a given hydrokinematic region in the surf zone), the approach taken here showed improved clustering of the optical intensities and smoother medians suggesting that this method is a sensible alternative to define hydrokinematic for individual waves. The optical intensities obtained at equivalent hydrokinematic regions could be re-projected into the timestack domain and then be used to estimate wave roller lengths for an irregular wave field; however, this is beyond the scope of this paper but will be investigated in a future publication.

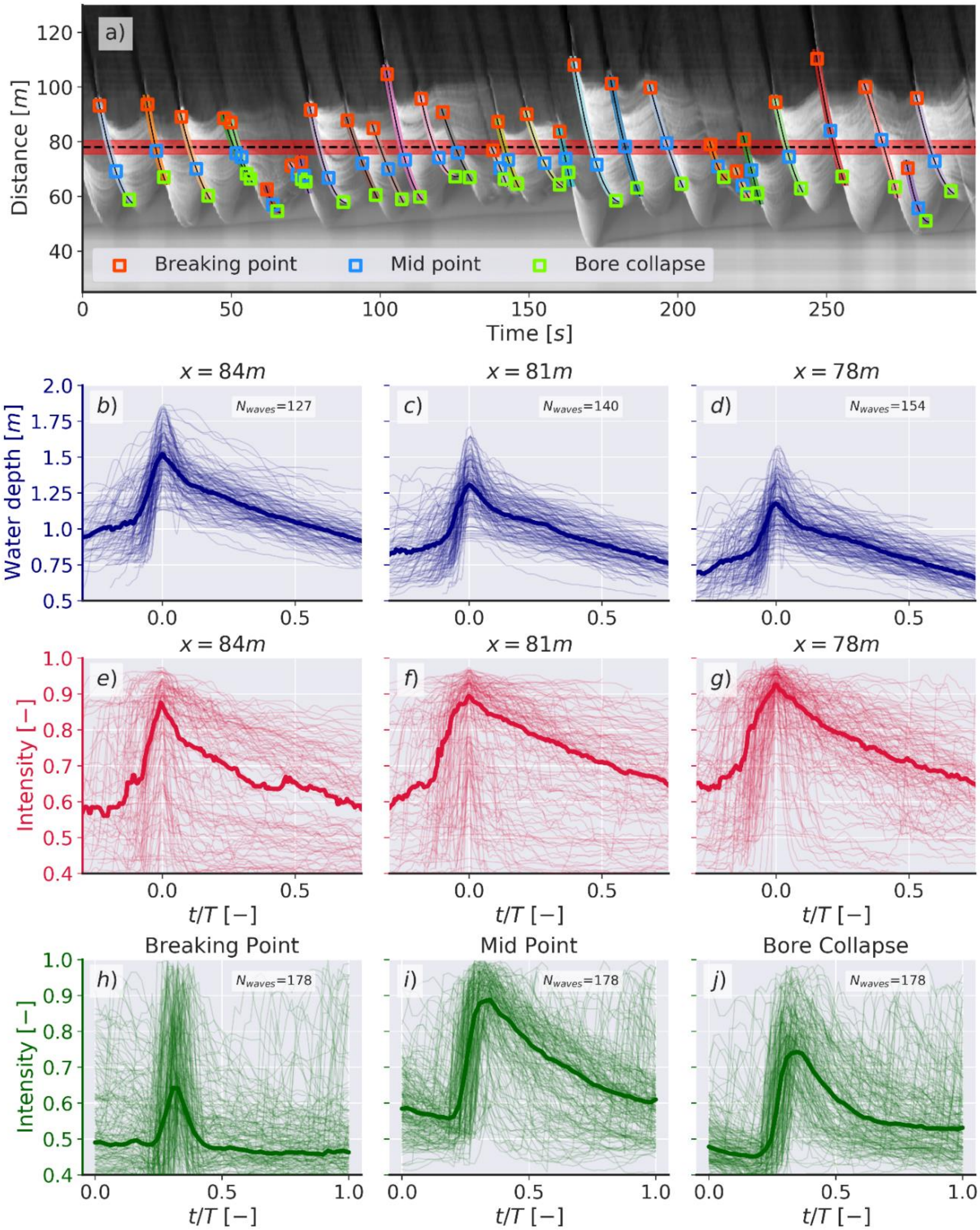

Figure 7. *Comparison between the phase-averaging method of Haller and Catálan (2009) at fixed spatial and at variable spatial (fixed hydrokinematic) locations for obtaining optical intensities from timestack images. a) Five minute subset of a timestack for OMB (300s). The*

dashed black line represents the location of the PT at x=78m and the red swath represents the spatial region used for averaging the pixel intensity signal (see panels b-d). The square markers indicate variable hydrokinematic regions for each tracked wave (see text for details). b, c, and d) Individual waves (thin lines) and medians (thick lines) for PT data at three different cross-shore locations (x=84m, x=81m, and x=78m). e, f, and g) Individual pixel intensities (thin lines) and respective medians (thick lines) at the same locations shown in b), c), and d). h, i, and j) Individual pixel intensity and respective medians (thick lines) at the three different wave-by-wave hydrokinematic locations.

4 Discussion

The novel remote sensing method for wave breaking detection and wave tracking in the surf zone presented here consists of two main components: 1) detecting wave breaking events and correcting errors using the data's true colour representation with machine learning techniques, and 2) clustering the detected breaking events into unique wave paths and obtaining optimal wave paths using an OLS model. The wave tracking step successfully tracked waves in the surf zone when applied to four sandy Australian beaches with varying morphodynamic characteristics, grazing angles, and light conditions. The two peak detection implementations (the cross-shore pixel intensity extrema and the horizontal Sobel operator) were accurate at detecting white pixel peaks that directly corresponded to the crests of breaking waves in the varying conditions in which data were collected. In the cases where the peak detection step misidentified pixel peaks, the machine learning colour comparison algorithm was able to correct errors due to its capability to learn from the data's true colour (See Figure 3). Although the wave crests of unbroken waves appeared clearly in some cases (e.g., Figure 4-a and c), there was not enough colour contrast between the wave crest and the adjacent undisturbed water to apply the same techniques used to distinguish between the crest of broken waves and undisturbed water, thus this algorithm remains restricted to breaking waves.

The most problematic step was the clustering of the identified wave breaking instances, in which the DBSCAN algorithm was highly sensitive to the minimum distance (eps) parameter. The optimal eps values were found after extensive trial and error, which was found to be time consuming, and there did not seem to be a consistent method to obtain the eps value nor any correlation to any environmental parameters (e.g., H_{m0} or T_p); for example, it varied from 0.005 in the OMB dataset to 0.15 in the SMB dataset. On the other hand, the minimum number of points of cluster parameter (n_{min}) was far more consistent between the datasets, with $n_{min} = 20$ working well for all data tested. Once the optimal eps and n_{min} were identified for each location, the number of wave paths being misclustered was significantly reduced. The RANSAC algorithm was effective at separating wave paths clustered as one wave in the cases where two waves merged (e.g., wave 6 in Figure 3-b), however, all other erroneous clustering required manual corrections. The average time required to run the method, assuming that the timestack image has already been obtained, the optimal eps and n_{min} are known, and there is no need for manual corrections, is less than 10 seconds on a standard laptop, which is at least one order of magnitude less than the Radon or Hough transforms methods. Initially, if the eps and n_{min} values are unknown, the method takes 10 to 15 minutes to produce good results for a five minute timestack depending on the users familiarity with the method. Once eps and n_{min} are known for a site, the time required to run the method would decrease for subsequent timestacks but is depending on the number of clustering errors that cannot be automatically fixed using RANSAC.

In general, the full method (i.e., wave breaking detection, colour machine learning, clustering, optimal wave path from OLS, and wave path correction) worked well for different incident wave conditions but was somewhat sensitive to light and grazing angle conditions, with better tracking results occurring under optimal imaging and light conditions (i.e., clear skies and high grazing angle). This is consistent with results from other remote sensing algorithms (e.g., Yoo et al., 2011, Catálan and Haller, 2008).

The optically derived wave speeds correlated poorly with the predictions from the linear wave theory ($r_{xy} = 0.68$) and there is a high intercept term in the regression, although the RMSE (0.69m.s^{-1}), MAE (0.55m.s^{-1}) and Bias (-0.002m.s^{-1}) are relatively low. The results showed that linear theory greatly underestimated observed wave speeds in deeper water depths and overestimated in shallower water depths. However, the water depth range in this paper was relatively small (of the order of 1m, see Figure 5-c), and these results may not hold for other depth ranges. Nonetheless, similar results have been observed by Postacchini and Brocchini (2014) (particularly the binned values seen in their Figure 20), and when the same regression analysis is completed for the data presented here (dashed green line in Figure 5-e), a coefficient of correlation (R^2) of 0.67 was found, which is close to the values reported by these authors.

The over-estimation of the wave speed by the theory at deeper water depths (outer surf zone) and subsequent underestimation at shallower water depths (inner surf zone) has been previously observed in natural surf zones (Suhayda and Pettigrew, 1977). There are physical mechanisms that would account for such differences, e.g., sea-swell waves propagating in the crest of infragravity waves propagate faster than it would be predicted by the theory and the reverse situation (sea-swell waves in the trough of an infragravity wave) is also possible (Tissier et al, 2015). In addition, some of the analysed data were very close to the surf-swash boundary (see Figure 5-a); a region where downrush and undertow could lead to a reduction of the wave speed that would not be accounted by the theory (Komar, 1978). Nonetheless, the exact physical mechanisms responsible for the observed differences are not fully understood and will be investigated in a subsequent publication.

Another factor that could contribute to the observed differences is vertical pixel misregistration due to non-optimal grazing angle and proximity of the camera to the timestack transect (Catálan and Haller, 2008). Unfortunately, no data were available to directly measure the vertical pixel misregistration in the dataset presented here. Considering that the measured horizontal RMSE for rectification in the OMB dataset was 0.11m, and considering that the vertical error is the same order of magnitude or less, the error in the wave speed calculations due to vertical pixel misregistration should be of the order of 1%. Moreover, the results for the comparison between times of travel of individual waves in the PT and wave path data presented in Section 3.1 (see Figure 6) are another strong suggestion that the trends seen in difference between the observed and theoretical wave speeds are not artefacts produced by errors in the rectification process.

In the comparison between optical intensities and surface elevation profiles, when the method described in Haller and Catálan (2009) was applied to the OMB dataset, no strong correlation between optical intensity and the surface elevations was observed when the phase-averaging was done at fixed spatial locations. When the method was adapted to take into account the variable spatial locations of hydrokinematic locations for individual waves, the correlation improved significantly. This is due to the fact that in natural surf zones, where the wave spectrum is rarely narrow, individual waves are at different stages of their hydrokinematic evolution at a given spatial location. It should be noted that, although a robust wave-by-wave cross-correlation method was used to align surface elevation profiles and optical intensities for individual waves, delays of up to 1 second between the wave crest and the maximum optical intensity were still observed in the data presented here, which could explain some the variability seen in Figure 7e-g.

These delays were mainly generated by strong white pixel peaks from foam being advected in the front of the wave crest that were an optical intensity maxima but did not necessarily corresponded to the wave crest in the pressure record. Although these delays could be responsible for some of the observed scattering, a high degree of optical variability would still be expected when extracting pixel intensity timeseries for individual waves at a fixed cross-shore location due to the wide bandwidth spectrum present in natural surf zones, as previously mentioned.

The method presented here has the potential to allow for novel investigations of several surf and swash zone process. To demonstrate the utility of the method we have examined the variability of instantaneous surf zone wave speeds and the variability of optical intensities associated with breaking waves. Potential other applications of this method include, but are not limited to: quantification of bore propagation and capture in the surf zone (e.g., Tissier et al., 2015, Garcia-Medina et al., 2017), investigation of the roles of reflected waves at the surf-swash boundary (Martins et al., 2017a), quantification of surf zone energy dissipation (as it provides a direct measurement of the fraction of broken waves in the surf zone) (e.g., Thornton and Guza, 1983, Baldock et al., 1998, Alsina et al., 2007), improved quantification of the interactions between incident wind-generated waves, infragravity waves, and run-up heights (e.g., de Bakker et al., 2016; de Moura and Baldock, 2017a; Padilla and Alsina, 2017), and as a direct input for bathymetry inversion methods (Holman et al., 2013; Catálan and Haller, 2008; van Dongeren et al., 2008; Bergsma et al., 2016).

5 Conclusions

This paper has presented a novel method for tracking individual waves in the surf zone using data derived from nearshore imagery. The hybrid computer vision, peak detection, and machine learning method was tested using data from four microtidal, swell-dominated, sandy

Australian beaches under varying incident wave, grazing angle, and light conditions, and for varying morphodynamic beach states. Results showed that the method successfully tracked waves in all four locations with better results obtained when grazing angles and light conditions were optimal (i.e., clear skies and high grazing angles). In these cases, the algorithm tracked all the broken waves and correctly identified all initial break point locations. The method was then used to derive instantaneous surf zone wave speeds which were compared to theoretical values derived from in-situ measurements. The results of this analysis showed that the theoretically predicted speeds agreed poorly with the optically derived speeds. Additionally, optical intensity profiles were extracted and compared to surface elevation profiles on a wave-by-wave basis. These results showed that phase-averaging in natural surf zones, or under wide bandwidth conditions, should be performed at equivalent hydrokinematic regions in the surf zone as identified on a wave-by-wave basis. The method developed in this paper has the potential to be used in novel investigations of several other surf zone phenomena that require wave tracking.

Acknowledgements

The field work at SMB, OMB, and WB in this study was funded by a University of Newcastle Faculty of Science and I.T. Strategic Initiatives Research Fund Grant 2014 to H.E.P.. The authors are grateful to Alex Atkinson, Andrew Magee, Annette Burke, Emily Kirk, Kaya Wilson, Madeleine Broadfoot, Michael Hughes, Mike Kinsela, Murray Kendall, Rachael Grant, Rebecca Hamilton, Samantha Clarke, and Tom Donaldson-Brown who assisted with the field data collection. C.E.S. is funded by a University of Newcastle Research Degree Scholarship (UNRS) and Central & Faculty scholarship (5050UNRS). The pressure transducers and video camera used for data collection in the SMB and WB experiments were kindly lent by Tom Baldock from the University of Queensland. The authors are also thankful to the Academic Research Computing

Support Team, particularly Aaron Scott, at the University of Newcastle for support with the I.T. infrastructure on which all video data pre-processing was undertaken, and to Bas Hoonhout who provided the original image rectification codes.

References

Aagaard, T., & Holm, J. (1989). Digitization of Wave Run-up Using Video Records. Journal of Coastal Research, 5(3), 547–551.

Almar, R., Michallet, H., Cienfuegos, R., Bonneton, P., Tissier, M., & Ruessink, G. (2014). On the use of the Radon Transform in studying nearshore wave dynamics. Coastal Engineering, 92, 24–30. https://doi.org/10.1016/j.coastaleng.2014.06.008

Alsina, J. M., & Baldock, T. E. (2007). Improved representation of breaking wave energy dissipation in parametric wave transformation models. Coastal Engineering, 54, 765–769. https://doi.org/10.1016/j.coastaleng.2007.05.005

Baldock, T. E., Holmes, P., Bunker, S., & Weert, P. Van. (1998). Cross-shore hydrodynamics within an unsaturated surf zone. *Coastal Engineering*, *34*, 173–196.

Battjes, J. A. (1988). Surf-Zone Dynamics. Annual Review of Fluid Mechanics, 20(1), 257–291. https://doi.org/10.1146/annurev.fl.20.010188.001353

Bergsma, E. W. J., Conley, D. C., Davidson, M. A., & O'Hare, T. J. (2016). Video-based nearshore bathymetry estimation in macro-tidal environments. Marine Geology, 374, 31–41. https://doi.org/10.1016/j.margeo.2016.02.001

Catálan, P. A., & Haller, M. C. (2008). Remote sensing of breaking wave phase speeds with application to non-linear depth inversions. Coastal Engineering, 55(1), 93–111. https://doi.org/10.1016/j.coastaleng.2007.09.010

Celebi, M. E. (2011). Improving the performance of k-means for color quantization. Image and Vision Computing, 29(4), 260–271. https://doi.org/10.1016/j.imavis.2010.10.002

CIE - Commission internationale de l'éclairage. (2017). CIE International Standards. Retrieved from http://www.cie.co.at/publications/international-standards de Bakker, A. T. M., Brinkkemper, J. A., Steen, F. Van Der, Tissier, M. F. S., & Ruessink, B. G. (2016). Cross-shore sand transport by infragravity waves as a function of beach steepness. Journal Of Geophysical Research: Earth Surface, 121, 1786–1799. https://doi.org/10.1002/2016JF003878.Abstract

de Moura, T. G. R., & Baldock, T. E. (2017). Remote sensing of the correlation between breakpoint oscillations and infragravity waves in the surf and swash zone. Journal of Geophysical Research: Oceans, 1–17. https://doi.org/10.1002/2016JC012233.Received

Ester, M., Kriegel, H.-P., Sander, J., & Xu, X. (2010). Density-Based Clustering Methods. Comprehensive Chemometrics, 2, 635–654. https://doi.org/10.1016/B978-044452701-1.00067-3

Fischler, M. A., & Bolles, R. C. (1981). Random sample consensus: a paradigm for model fitting with applications to image analysis and automated cartography. Communications of the ACM, 24(6), 381–395. https://doi.org/10.1145/358669.358692

Freedman, D., & Diaconis, P. (1981). On the histogram as a density estimator:L 2 theory. Zeitschrift Für Wahrscheinlichkeitstheorie Und Verwandte Gebiete, 57(4), 453–476. https://doi.org/10.1007/BF01025868

Haller, M. C., & Catalán, P. A. (2009). Remote sensing of wave roller lengths in the laboratory. Journal of Geophysical Research: Oceans, 114(7), 1–19. https://doi.org/10.1029/2008JC005185

Holland, K. T., Holman, R. A., Lippmann, T. C., Stanley, J., Member, A., & Plant, N. (1997). Practical Use of Video Imagery in Nearshore Oceanographic Field Studies. IEEE Journal of Oceanic Engineering, 22(1), 81–92.

Holman, R., Plant, N., & Holland, T. (2013). CBathy: A robust algorithm for estimating nearshore bathymetry. Journal of Geophysical Research: Oceans, 118(5), 2595–2609. https://doi.org/10.1002/jgrc.20199

Holthuijsen, L. H. (2010). Waves in Oceanic and Coastal Waters. Cambridge University Press.

Hoonhout, B. M., Radermacher, M., Baart, F., & Maaten, L. J. P. Van Der. (2015). An automated method for semantic classification of regions in coastal images. Coastal Engineering, 105, 1–12. https://doi.org/10.1016/j.coastaleng.2015.07.010

ITSEEZ. (2014). Open Source Computer Vision Library.

Kirby, J. T., & Dalrymple, R. A. (1986). An approximate model for nonlinear dispersion in monochromatic wave propagation models. Coastal Engineering, 9(6), 545–561. https://doi.org/10.1016/0378-3839(86)90003-7

Komar, P. D. (1976). Beach Processes and Sedimentation. 2nd Edition. Prentice-Hall.

Lou, R. M., Cui, G., & Li, C. (2006). Uniform colour spaces based on CIECAM02 colour apperance model. Color Research and Application, 31(4), 320–330. https://doi.org/10.1002/col.20227

Martins, K., Blenkinsopp, C. E., Almar, R., & Zang, J. (2017a). The influence of swash-based reflection on surf zone hydrodynamics: a wave-by-wave approach. Coastal Engineering, 122(January), 27–43. https://doi.org/10.1016/j.coastaleng.2017.01.006

Martins, K., Blenkinsopp, C. E., Power, H. E., Bruder, B., Puleo, J. A., & Bergsma, E. W. J. (2017b). High-resolution monitoring of wave transformation in the surf zone using a LiDAR scanner array. Coastal Engineering, 128(July), 37–43. https://doi.org/10.1016/j.coastaleng.2017.07.007

Masselink, G., & Puleo, J. A. (2006). Swash-zone morphodynamics. Continental Shelf Research, 26(5), 661–680. https://doi.org/10.1016/j.csr.2006.01.015

NSW Office of Environment and Heritage. (2017). NSW Nearshore Wave Forecast tool. Retrieved from http://www.nswaves.com.au/

Padilla, E. M., & Alsina, J. M. (2017). Transfer and dissipation of energy during wave group propagation on a gentle beach slope. Journal of Geophysical Research: Oceans, 122(8), 6773–6794. http://doi.org/10.1002/2017JC012703

Pedregosa, F., Varoquaux, G., Gramfort, A., Michel, V., Thirion, B., Grisel, O., … Duchesnay, E. (2011). Scikit-learn: Machine Learning in Python. Journal of Machine Learning Research, 12, 2825–2830.

Postacchini, M., & Brocchini, M. (2014). A wave-by-wave analysis for the evaluation of the breaking-wave celerity. Applied Ocean Research, 46, 15–27. https://doi.org/10.1016/j.apor.2014.01.005

Power, H. E., Hughes, M. G., Aagaard, T., & Baldock, T. E. (2010). Nearshore wave height variation in unsaturated surf. Journal of Geophysical Research: Oceans, 115(8), 1–15. https://doi.org/10.1029/2009JC005758

Power, H. E., Holman, R. A., & Baldock, T. E. (2011). Swash zone boundary conditions derived from optical remote sensing of swash zone flow patterns. *Journal of Geophysical Research: Oceans*, *116*(6), 1–13. http://doi.org/10.1029/2010JC006724

Power, H. E., Hughes, M. G., & Baldock, T. E. (2015). A novel method for tracking individual waves in the surf zone. Coastal Engineering, 98, 26–30. https://doi.org/10.1016/j.coastaleng.2015.01.006

Smith, T., & Guild, J. (1931). The C.I.E. colorimetric standards and their use. Transactions of the Optical Society, 33(3), 73–134. https://doi.org/10.1088/1475-4878/33/3/301

Sobel, I. (1990). An isotropic 3 by 3 image gradient operator. Machine Vision for Three-Dimensional Sciences, 1(1), 23–34. https://doi.org/10.13140/RG.2.1.1912.4965

Suhayda, J. N., & Pettigrew, N. R. (1977). Observations of wave height and wave celerity in the surf zone. Journal of Geophysical Research, 82(9), 1419–1424. https://doi.org/10.1029/JC082i009p01419

Thornton, E. B., & Guza, R. T. (1983). Transformation of Wave Height Distribution. Journal of Geophysical Research, 88(C10), 5925–5938.

Tissier, M., Bonneton, P., Michallet, H., & Ruessink, B. G. (2015). Infragravity-wave modulation of short-wave celerity in the surf zone. Journal of Geophysical Research: Oceans, 120(10), 6799–6814. https://doi.org/10.1002/2015JC010708

van Dongeren, A., Plant, N., Cohen, A., Roelvink, D., Haller, M. C., & Catalán, P. (2008). Beach Wizard: Nearshore bathymetry estimation through assimilation of model computations and remote observations. Coastal Engineering, 55(12), 1016–1027. https://doi.org/10.1016/j.coastaleng.2008.04.011

Wright, L. D., & Short, A. D. (1984). Morphodynamic variability of surf zones and beaches: A synthesis. Marine Geology, 56(1–4), 93–118. https://doi.org/10.1016/0025-3227(84)90008-2

Yoo, J., Fritz, H., Haas, K., Work, P., & Barnes, C. (2010). Depth Inversion in the Surf Zone with inclusion of wave nonlinearity using video-derived celerity. Journal of Waterway, Port, Coastal and Ocean Engineering, 137(April), 95–106. https://doi.org/10.1061/(ASCE)WW.1943-5460.0000068.